SIMULATION AND ANALYSES OF A GENERIC WING-BODY CONFIGURATIONS IN SUPERSONIC FLOW

Gustavo Bono[a] and Armando M. Awruch[b]

[a]*Federal University of Rio Grande do Sul, Graduate Program in Mechanical Engineering, Av. Sarmento Leite 425, 90050-170 Porto Alegre, RS, Brazil, bonogustavo@gmail.com, http://www.mecanica.ufrgs.br/promec*
[b]*Federal University of Rio Grande do Sul, Applied and Computacional Mechanical Center, Av. Osvaldo Aranha 99, 90035-190 Porto Alegre, RS, Brazil, amawruch@ufrgs.br, http://www.ppgec.ufrgs.br/cemacom*

Keywords: Supersonic flow, adaptive mesh strategy, wing-body configuration, finite element method.

Abstract. Viscous and non-viscous supersonic flow simulations over a wing-body configuration are presented in this work. The numerical analysis is carried out using the Finite Element Method with an explicit one-step Taylor-Galerkin scheme and adaptive unstructured meshes employing linear tetrahedral elements. The calculations are performed with different Mach numbers (M = 2.3 and 4.63) and angles of attack (alpha = 6.2 deg and 11.1 deg). Finally, the structure of the flow field is discussed for each case and computational results are compared to available experimental data.

1   INTRODUCTION

Current and expected developments in space transportation have led to growing interest in new space vehicles. Several expendable and partially or fully reusable concepts are discussed or already planned. These new vehicles require essential improvements over current vehicles in order to ensure economic viability and to fulfill mission and safety constraints.

Over the past forty years, there has been an intense research activity in the area of Computational Fluid Dynamics (CFD). A large proportion of this activity has been driven by the aerospace industry, with its requirements for highly accurate solutions at minimum computational cost. Recent developments in numerical methods and their applications permit to solve complex and realistic geometries and configurations for compressible flows. The demand to solve finely detailed models has challenged many researchers to come up with new and efficient tools. The spatial adaptation method has been demonstrated as an efficient means for obtaining solutions to the Euler and Navier-Stokes equations.

A numerical investigation is conducted to determine the structure of the flow field and the main aerodynamic characteristics over a wing-body (W-B) configuration at high supersonic speeds. The wing-body configuration could be compared with some supersonic transport vehicles, aerospace vehicles, guided missiles or a generic Unmanned Combat Air Vehicle (UCAV).

The three-dimensional flow on the W-B configuration is complex and it contains a variety of interactions. To obtain an accurate solution, it is evident that considerable benefit could be achieved if the mesh employed is adapted to the solution in an optimal manner. Adaptive meshing is a powerful tool in CFD that substantially enhances the accuracy, efficiency, and automation of the numerical methods. In this work, an adaptive mesh method is employed to enhance the definition of complex flow features over the W-B configuration.

The purpose of this paper is to report results of numerical tests analyzing the aerodynamic effects of inviscid and viscous flows about a wing-body configuration. A three-dimensional Euler/Navier-Stokes solver is used jointly with a spatial refinement technique. Simulations are performed for two supersonic Mach number and for two angles of attack. The accuracy of the computational techniques developed and applied in this study is demonstrated through extensive comparison with available experimental data.

2   GEOMETRY AND CHARACTERISTICS OF THE FLOW FIELD

Numerous experimental as well as numerical studies have been conducted over delta wing and slender body to get an understanding of these flow fields. Figure 1 (taken from Pirzadeh, 2003) illustrates the characteristic vortical flow field found above a non-cambered sharp leading edge delta wing and a section of a slender body operating at moderately high angle of attack. The dominant feature of the delta wing is a pair of counter-rotating vortices created at the sharp leading edge flowing over the upper (leeward) surface of the wing. The formation of vortices is essentially triggered by the separation of flow and subsequent shedding of vorticity from the lifting surface. Although vortex flows are inherently viscous, the bulk of the swirling flow outside the boundary layer can be assumed as being non-dissipative. Therefore, the Euler equations are capable to compute the formation of vortices from the sharp leading edges of lifting surfaces.

The free stream flow moving over these primary vortices (*PV*) is entrained towards the wing, where it is attached (PRL) to the upper surface. It is then swept outboard, beneath the primary vortices. The large adverse pressure gradient between the primary and the leading edge causes the attached flow to separate (SSL), creating a secondary vortex (*SV*). This

secondary vortex is smaller and weaker than the primary vortex, turning in the opposite sense of the primary vortex. The presence of the secondary vortex moves the primary vortex upward and inboard. This shift is greater if the boundary layer on the upper surface is laminar since flow separation occurs earlier and forms a larger secondary vortex. Outboard of the secondary vortex the flow reattaches (SRL) and continues moving towards the leading edge. As the flow reaches the leading edge it is entrained into the vortex sheet that is separated from the lower surface and it feeds the primary vortices. The underlying cause of these additional vortices is viscous-dominated and, obviously, cannot be predicted with the Euler equations. When the secondary vortex is relatively strong, may lead to another adverse lateral pressure gradient inboard of the secondary vortex resulting in a third separation and a tertiary vortex. The tertiary vortex is not illustrated in Figure 1.

The location of the flow separation lines, reattachment lines and the core of the vortices are known to be a complex function of the free stream Mach number, leading edge sweep angle, leading edge shape, surface camber and the Reynolds number. The secondary separation line (SSL), in contrary to the primary separation line (PSL) is not fixed. For sharp leading edged delta wings the Reynolds number has little effect on the structure of the vortices.
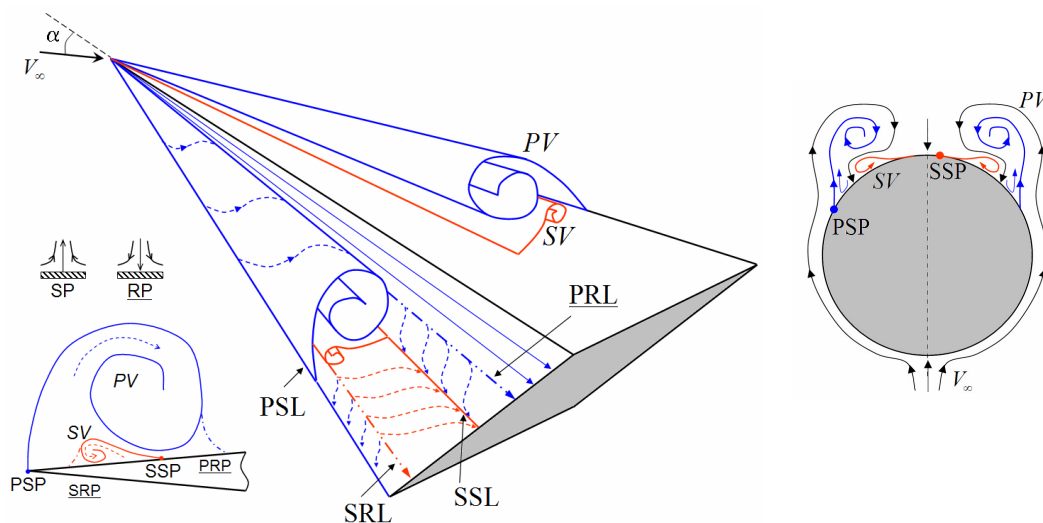
Figure 1: Structure of the flow over a sharp leading edge delta wing at intermediate angle of attack, where *PV*=primary vortex, *SV*=secondary vortex, P/SSL=primary/secondary separation line, P/SRL=primary/secondary reattachment line, P/SSP=primary/secondary separation point, P/SRP=primary/secondary reattachment point, SP=separation point and RP=reattachment point

In the body section, the flow topology is similar to that shown for the delta wing, however, the primary separation point (PSP) is not fixed. Both, the primary and secondary separation points (SSP), are strongly affected by the state of the boundary layer, more specifically by the Reynolds number. Cross-flow separation, as depicted in Figure 1 (taken from Bertin, 1994) occurs when the flow from windward to leeward separates into a coiled vortex. This primary vortex reattaches near the symmetry plane, often generating a secondary vortex inboard. The proper captures of this secondary vortex, and even possible tertiary vortices, is essential to correctly reflect the physics driving the primary vortex, in its formation and shedding process. The strength and impact of these vortical constructions increase with the angle of attack.

3   THE GOVERNING EQUATIONS

Let $\Omega \subset R^{n_{sd}}$ and (0,T) be the spatial and temporal domains, respectively, where $n_{sd} = 3$ is

the number of space dimensions, and let Γ denote the boundary of Ω. The spatial and temporal coordinates are denoted by $\mathbf{x}$ and t. The Navier-Stokes equations describe the motion of Newtonian compressible perfect fluids, and they are written here in their dimensionless form with no source terms as follows

$$\partial_t \rho + \operatorname{div}(\rho \mathbf{u}) = 0$$
$$\partial_t (\rho \mathbf{u}) + \operatorname{div}(\rho \mathbf{uu}) = -\operatorname{grad} p + \operatorname{div} \sigma \qquad (1)$$
$$\partial_t (\rho e) + \operatorname{div}(\rho e \mathbf{u}) = -\operatorname{grad} p + \operatorname{div}(\sigma \cdot \mathbf{u}) + \operatorname{div}(\kappa \operatorname{grad} T)$$

where, $\sigma = \lambda(\operatorname{div}\mathbf{u})\mathbf{I} + 2\mu\mathbf{D}$ is the stress tensor, $\mathbf{I}$ is the unit tensor, $\mathbf{D}$ is the rate-of-strain tensor, λ and μ are the volumetric and dynamic viscosity coefficients, respectively, κ is the thermal diffusivity. With appropriate boundary conditions, equations (1) defines the velocity field $\mathbf{u}$, the specific mass ρ and total energy e. The perfect gas law and internal energy i are given by the following equations

$$p = (\gamma - 1)\rho i, \qquad i = c_v T = e - \frac{1}{2} v_i v_i \qquad (2)$$

where p is the pressure, T is the temperature and $\gamma = c_p / c_v$, which is the specific heat ratio, is assumed to be constant and equal to 1.4 for air.

The governing equation can be also written in a compact form as

$$\frac{\partial \mathbf{U}}{\partial t} + \frac{\partial \mathbf{F}_i}{\partial x_i} + \frac{\partial \mathbf{G}_i}{\partial x_i} = 0 \qquad (3)$$

where $\mathbf{U}$ is the unknown vector of the conservation variables, $\mathbf{F}_i$ and $\mathbf{G}_i$ are, respectively, the advective and diffusive flux vectors.

4 COMPUTATIONAL METHOD

In this work, we will only be concerned with the solution of steady flows. These solutions will be achieved by advancing the time dependent governing equations until steady conditions are obtained. An explicit one-step scheme is employed for solving the compressible inviscid/viscous flow problems. In Finite Element Method (FEM) the flow field is subdivided into a set of non-overlapping elements which cover the whole domain without gaps.

The results presented in this paper have been produced using tetrahedral finite elements and the Euler as well as Navier-Stokes solvers, with an adaptive mesh refinement technique.

4.1 Algorithm: discretization in time and in space

The one-step scheme is similar to that presented by Donea (1984). To develop the scheme, we consider a Taylor expansion of the unknown variables $\mathbf{U}(\mathbf{x}, t)$ in time $t = t^{n+1}$. The Taylor series including the first and second derivatives, and substituting the implicitness parameters with $s_1 = s_2 = 1/2$, the following expression is obtained

$$\Delta \mathbf{U}^{n+1} = \Delta t \left(\frac{\partial \mathbf{U}^n}{\partial t} + \frac{1}{2} \frac{\partial \Delta \mathbf{U}^{n+1}}{\partial t} \right) + \frac{\Delta t^2}{2} \left(\frac{\partial^2 \mathbf{U}^n}{\partial t^2} + \frac{1}{2} \frac{\partial^2 \Delta \mathbf{U}^{n+1}}{\partial t^2} \right) \qquad (4)$$

with $\Delta \mathbf{U}^{n+1} = \mathbf{U}^{n+1} - \mathbf{U}^n$, $\mathbf{U}$ is the unknown vector of the conservation variables, the time step

$\Delta t = t^{n+1} - t^n$, *n* and *n+1* indicates *t* and *t+Δt*, respectively. More details can be found in Bono (2008). Substituting first and second derivatives, taking into account the governing equation (3) into equation (4), and neglecting higher order terms, it is obtained

$$\Delta \mathbf{U}_{I+1}^{n+1} = \Delta t \left[-\frac{\partial \mathbf{F}_i}{\partial x_i}^n - \frac{\partial \mathbf{G}_i}{\partial x_i}^n + \frac{\Delta t}{2} \frac{\partial}{\partial x_k} \left(\mathbf{A}_k^n \frac{\partial \mathbf{F}_i}{\partial x_i}^n \right) \right] +$$
$$+ \frac{\Delta t}{2} \left[-\frac{\partial \Delta \mathbf{F}_{iI}}{\partial x_i}^{n+1} - \frac{\partial \Delta \mathbf{G}_{iI}}{\partial x_i}^{n+1} + \frac{\Delta t}{2} \frac{\partial}{\partial x_k} \left(\mathbf{A}_k^n \frac{\partial \Delta \mathbf{F}_{iI}}{\partial x_i}^{n+1} \right) \right]$$

(5)

where *I* is an iteration counter, $\Delta \mathbf{F}_i^{n+1} = \mathbf{F}_i^{n+1} - \mathbf{F}_i^n$, $\Delta \mathbf{G}_i^{n+1} = \mathbf{G}_i^{n+1} - \mathbf{G}_i^n$ and $\mathbf{A}_i$ is the convection Jacobian defined as $\mathbf{A}_i = \partial \mathbf{F}_i / \partial \mathbf{U}$ (Hughes and Tezduyar, 1984). In expression (5), the variables at time level *n+1* are involved in the left and right sides of the equation; therefore it is necessary to use an iterative scheme.

Applying the classical Bubnov-Galerkin weighted residual method in the context of the finite element method (FEM) to equation (5), the spatial discretisation is obtained. The computational domain was divided into a finite number of linear tetrahedral elements. The consistent mass matrix, **M**, is substituted by the lumped mass matrix, $\mathbf{M}_L$, and then these equations are solved with an explicit scheme. The explicit matrix form of equations (5) can be found in Bono (2008).

The explicit character of the algorithm implies that it will be subjected to the Courant-Friedrichs-Lewy stability criterion. The local stability condition for element *E* is given by

$$\Delta t_E = CS \frac{L_E}{a + \left(v_i v_i \right)^{1/2}}$$

(6)

where L_E is a characteristic dimension of the element, *a* is the sound speed and *CS* is a safety coefficient (in this work the coefficient adopted were CS = 0.1).

At supersonic speeds, an additional numerical damping is necessary to capture shocks and to smooth local oscillations in the vicinity of shocks. An artificial viscosity model, as proposed by Argyris et al. (1990), due to its simplicity and efficiency in terms of CPU time, is adopted here. The artificial viscosity is added explicitly to the non-smoothed solution as follows

$$\mathbf{U}_s^{n+1} = \mathbf{U}^{n+1} + \mathbf{M}_L^{-1} \left(\sum_{ele} \text{CFL CAF } S_{ele} \left[\mathbf{M} - \mathbf{M}_L \right]_{ele} \mathbf{U}_{ele}^n \right)$$

(7)

where $\mathbf{U}_s^{n+1}$ and $\mathbf{U}^{n+1}$ are the smoothed and non-smoothed solutions at $t + \Delta t$, respectively. $\mathbf{M}_L$ is the assembled lumped mass matrix, **M** is the consistent mass matrix at element level, *ele* is an index referred to a specific element, $\text{CFL} = \Delta t / \Delta t_E$ is the local Courant-Friedrichs-Lewy number, CAF is an artificial damping coefficient given by the user, S_{ele} is a pressure sensor at element level obtained as an average of nodal values S_i. Values of S_i are components of the following assembled global vector

$$S_i = \sum_{ele} \frac{\left| \left(\mathbf{M} - \mathbf{M}_L \right)_{ele} \mathbf{p} \right|_i}{\left[\left| \mathbf{M} - \mathbf{M}_L \right|_{ele} \mathbf{p} \right]_i}$$

(8)

where **p** is the vector containing the nodal values of the pressure of a specific element *ele*, the $|\cdot|$ indicates that absolute values of the corresponding terms must be taken. The constant CAF must be specified with care in order to avoid interferences of artificial and physical viscosities. In this work CAF = 1.0 for inviscid flows and 0.7 for viscous flows were adopted.

4.2 Adaptive mesh refinement method

The unstructured mesh adaptation has the potential to give numerically accurate and computationally efficient solutions, because the mesh is only locally refined at the places of interest. An adaptive mesh strategy basically is characterized by an error indicator, an adaptive criterion and a refinement scheme.

The error indicator is used to identify the characteristics and behavior of the numerical solutions in order to determine regions of the computational domain where a refinement process is necessary, looking for an accurate solution. In this work, these error indicators take into account regions with low velocity components (LV), change in the direction of velocity components (DV), velocity gradients (VG), pressure gradients (PG) and specific mass gradients (RG). The criterion for mesh adaptation is based in the normal distribution of the error indicators and their mean values and standard deviation. The adaptive process was performed using the *h*-refinement method. Elements refined are divided in eight new elements; this type of refinement is defined as a regular refinement, and it is represented by 1:8. To close the refinement scheme and to avoid hanging nodes, it is necessary to perform irregular refinements in neighbor elements, represented by 1:2, 1:3 or 1:4. Elements having less than four edges divided by new nodes, created as a consequence of the adaptation scheme applied to their neighbor elements, are submitted to irregular refinements. However, if an element has four or more edges divided by new nodes, it is submitted to a regular refinement. Details of the error indicators, mesh adaptation and the refinement process can be found in Popiolek and Awruch (2006).

This adaptive scheme has been validated with respect to analytical and experimental results for several regimes of incompressible and compressible flows (Popiolek and Awruch, 2006; Bono, Popiolek and Awruch, 2007; Bono, 2008).

5 NUMERICAL RESULTS

In this section, results are presented for a W-B configuration for steady flows. Jernell (1971) obtained experimental results for a W-B configuration with varying Mach number (2.30 to 4.63) and different angles of attack (0 deg to 11.1 deg).

A three-view drawing of the model is given in Figure 2. The front part of the fuselage is generated with the criteria of Haack (Jernell, 1971), which predicts the profile required for minimizing the wave drag. The remaining aft section of the fuselage is cylindrical. The wing has a delta planform of 65° leading edge sweep and a symmetrical double-wedge airfoil of 6 percent thickness. In this study, Euler and Navier-Stokes equations are used. Firstly, results obtained for an inviscid flow (WBeu) are presented and later on results obtained in viscous flow (WBns) with the free stream Reynolds number equal to Re = 1×10^5 are shown. The different cases computed here are listed in Table 1. It should be noted that in both examples supersonic flows are considered.

Only a half of the W-B configuration is modeled and the domain is shown in Figure 3, being the dimensions R = 30, L = 55 and L_1 = 15.5. The free stream conditions are: velocity $V_\infty = \left(M_\infty \cos\alpha; M_\infty \,\text{sen}\,\alpha; 0 \right)$, specific mass $\rho_\infty = 1.0$, total energy $e_\infty = 4.4307$

$\left(M_{\infty} = 2.30\right)$ or 12.5041 $\left(M_{\infty} = 4.63\right)$ and pressure $p_{\infty} = 0.71428$. The inflow boundary conditions were applied in the plane defined by the edges AB and BDEF. In ACEF symmetric boundary conditions are applied and the non slip boundary condition (viscous cases) or zero normal velocity (inviscid cases) are imposed over the W-B configuration. Finally, in CD no boundary conditions are prescribed. The values of the free stream conditions are taken as initial conditions and implemented in all the nodes of the domain, except in the nodes over the W-B configuration.
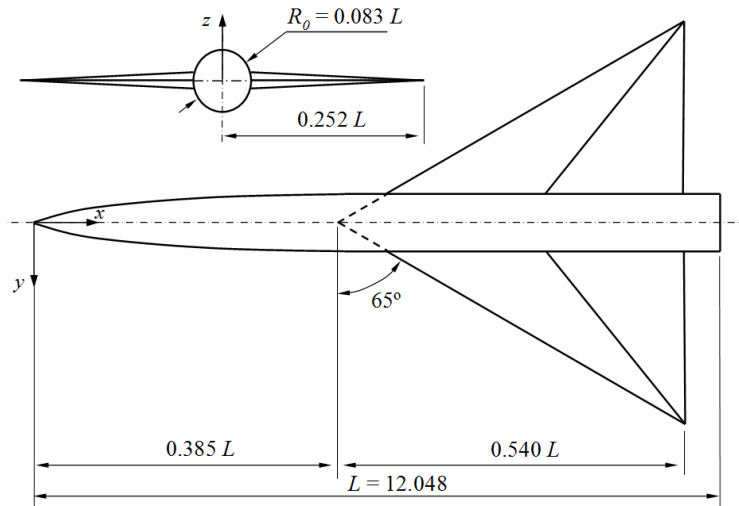
Figure 2: Schematic representation wing-body model

		Angle of attack [deg]	
		6.2	11.1
Mach	2.30	WBns3	WBeu1 WBns1
	4.63	WBeu2 WBns2	WBns4

Table 1: W-B cases computed in this example, where *eu* = inviscid flow and *ns* = viscous flow.
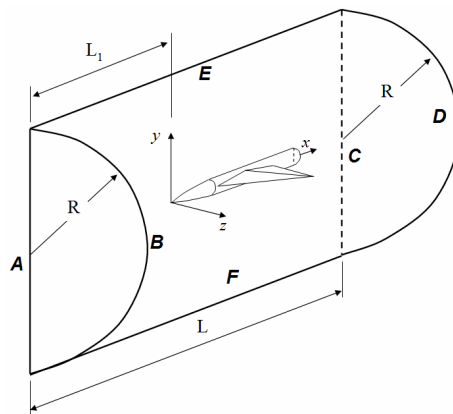
Figure 3: Computational domain

The first simulations for all cases are performed using the same initial mesh consisting of 194501 tetrahedral. The identification of each example, the number of nodes (*nno*), the number of elements (*nele*), the number of nodes on the W-B configuration (*nnoCS*), the maximum edge length (L_{max}), the minimum edge length (L_{min}) and the minimum time step (Δt) are described in Table 2.

cases	mesh	*nno*	*nele*	*nnoCS*	L_{max}	L_{min}	Δt
M=2.30	WBns3	37061	194501	6877	8.08	7.47×10^{-3}	2×10^{-4}
$\alpha=6.2°$	WBns3R1	217212	1193165	27124	8.03	3.73×10^{-3}	1×10^{-4}
	WBeu1	37061	194501	6877	8.08	7.47×10^{-3}	2×10^{-4}
	WBeu1R1	118082	659121	10422	8.08	3.73×10^{-3}	1×10^{-4}
M=2.30	WBeu1R2	364996	2093370	14635	8.08	1.87×10^{-4}	5×10^{-5}
$\alpha=11.1°$	WBns1	37061	194501	6877	8.08	7.47×10^{-3}	2×10^{-4}
	WBns1R1	214427	1177222	27124	8.08	3.73×10^{-3}	1×10^{-4}
	WBeu2	37061	194501	6877	8.08	7.47×10^{-3}	1×10^{-4}
M=4.63	WBeu2R1	124897	697869	10906	8.08	3.73×10^{-3}	1×10^{-4}
$\alpha=6.2°$	WBns2	37061	194501	6877	8.08	7.47×10^{-3}	1×10^{-4}
	WBns2R1	187406	1055245	13647	8.03	4.69×10^{-3}	8×10^{-5}
M=4.63	WBns4	37061	194501	6877	8.08	7.47×10^{-3}	1×10^{-4}
$\alpha=11.1°$	WBns4R1	185123	1044230	12864	8.03	4.69×10^{-3}	8×10^{-5}

Table 2: Numerical parameters for the W-B configuration.

The adaptive mesh technique is employed in all cases with the following errors indicators: VG, PG and RG for the inviscid cases and LV, DV, VG, PG and RG for the viscous cases. More details can be found in Bono (2008). The first and second refinements were identified as R1 and R2, respectively.

5.1 Inviscid cases

In Figure 4, the specific mass distributions obtained with the initial mesh (Wbeu1) and final (Wbeu1R2) mesh (obtained after two refinement levels in the cases of Mach number 2.30 and angle of attack 11.1 deg) are shown. The improvement in the definition of the principal flow features (expansion fan and shock wake) on the adapted mesh is clearly observed.

Figure 5 shows Mach number distribution and meshes in the plane perpendicular to the W-B model centerline, for $x_b/L = 0.80$, where x_b is the axial distance, which is normalized with respect to the body length L. The flow expands around the leading edge onto the upper surface of the wing, causing the formation of a relative weak shock at about 70% of the semispan. The initial mesh is not able to capture the shock wave formed on the upper surface of the wing and on the lower part the W-B configuration.

The distribution of the pressure coefficient across the delta wing at four different locations ($2y/b$) across the span is compared with experimental results presented by Jernell (1971) in Figure 6. Numerical results are obtained employing the WBeu1R2 mesh. In the location, *2y/b*,

y is the spanwise distance, normalized with respect to the semispan *b/2*. Excellent agreements between the experimental and numerical results with two refinement levels are obtained.
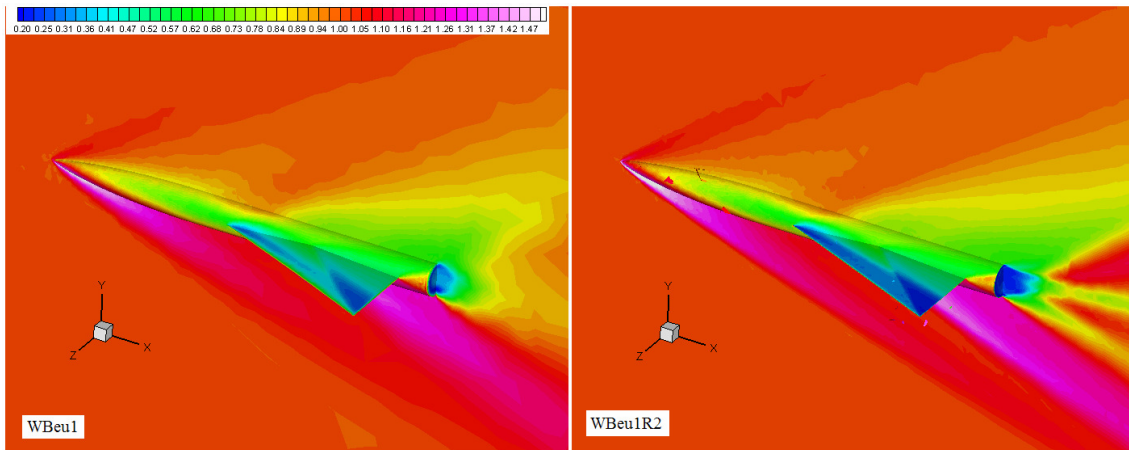
Figure 4: Specific mass contours for the initial (WBeu1) and final (WBeu1R2) meshes for M = 2.30 and alpha = 11.1°
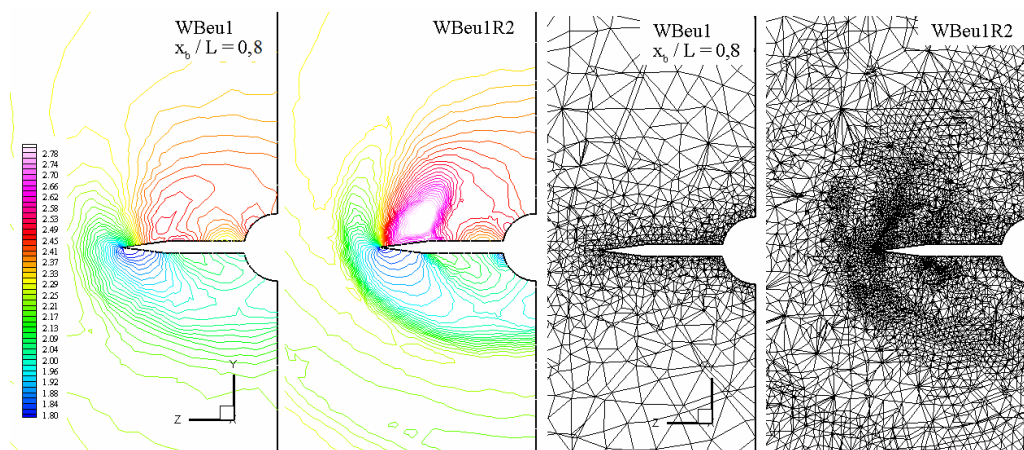
Figure 5: Mach number distribution and meshes in x_b/L = 0.80 for M = 2.30 and alpha = 11.1°

The pressure coefficient distribution at four different sections is shown in Figure 7 for WBeu2R1 mesh. The level of agreement between the numerical prediction and experimental results (Jernell, 1971) is certainly acceptable considering that only one refinement level is employed.

The specific mass distribution on the three views of the W-B configuration WBeu1R2 (M=2.30 and α=11.1°) and WBeu2 (M=4.63 and α=6.2°) are shown in Figure 8. The letters U and L indicate upper and lower, respectively. The compression and expansion regions on the wing and body are clearly identified in both examples. The distribution on the body is strongly influenced in the wing-body intersection. On the lower surface of the wing, the specific mass is initially compressed (the specific mass increase) in the front of the wing due to the shock wave in the leading edge. After this region the flow is expanding through an expansion fan. In the front of the body the flow is more compressed in the mesh WBeu2 with M = 4.63 than the mesh WBeu1R2 with M = 2.30.
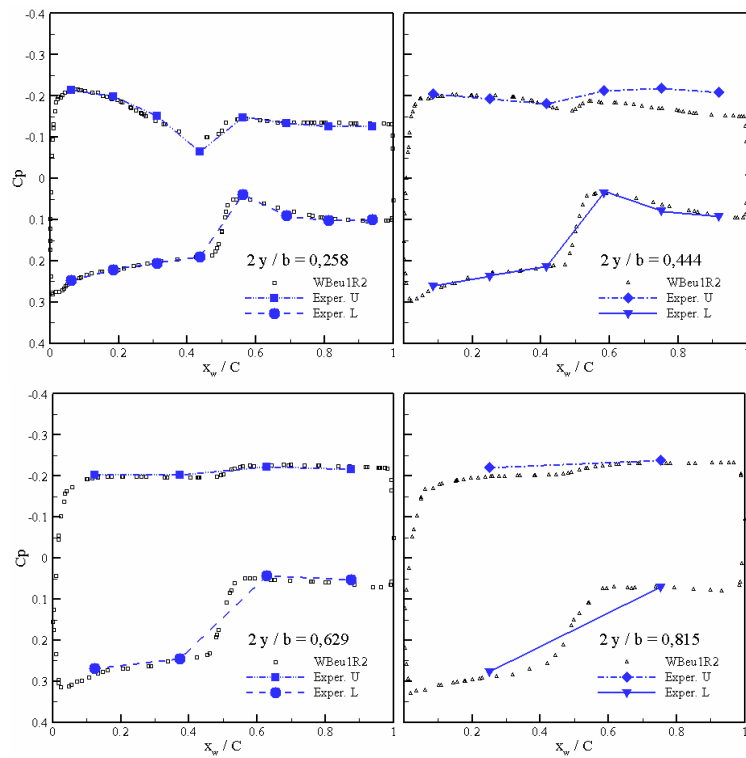
Figure 6: Pressure coefficient over a W-B configuration. Comparison between numerical prediction and an experimental work at different sections for the WBeu1R2 mesh
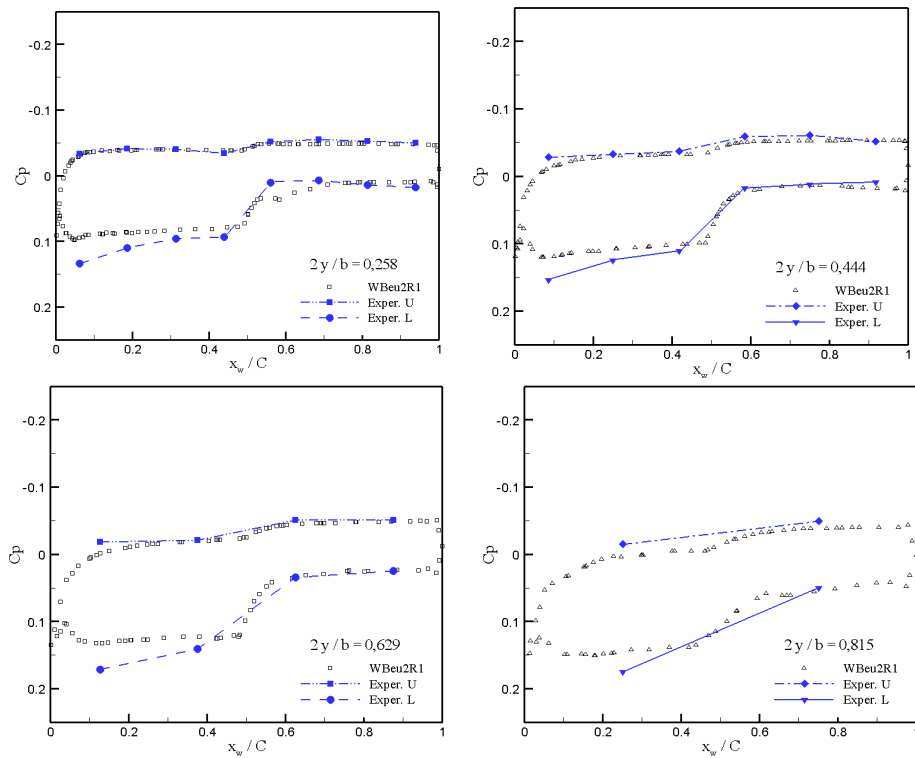
Figure 7: Pressure coefficient over a W-B configuration. Comparison between numerical prediction and an experimental work at different sections for the WBeu2R1 mesh
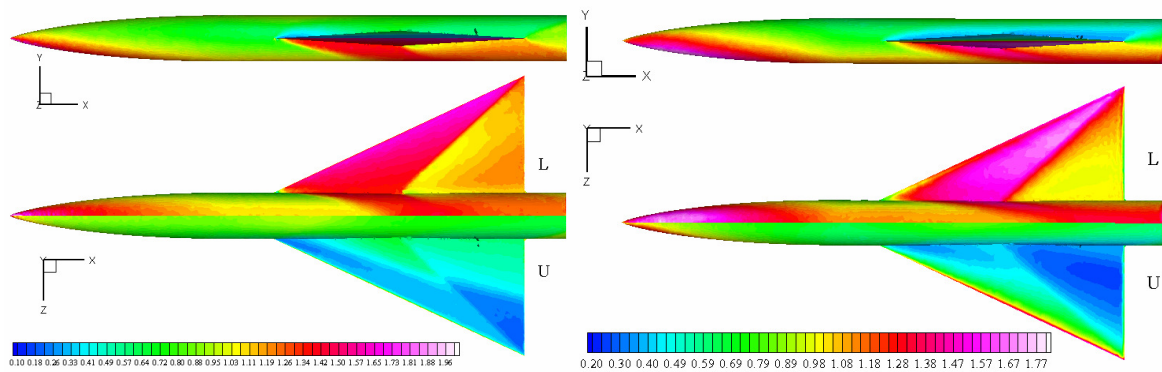
Figure 8: Specific mass distribution over a W-B configuration for WBeu1R2 (left) and WBeu2 (right)

The region with the minimum value of the specific mass is located on the upper surface and near the leading edge for the mesh WBeu1R2 (M=2.30 and α=11.1°), however, for the mesh WBeu2 (M=4.63 and α=6.2°) the region with the minimum value of ρ is located approximately in the middle of the delta wing.

5.2 Viscous cases

The Mach number distribution over the W-B configuration for different stations (x_b/L=0.1 to 1.2 with steps equal to 0.1) are shown in Figure 9 for all Mach number-angle of attack combinations (see Table 1). It should be noted that in regions with low speed, the Mach number is higher in the cases where the angle of attack is equal to 11.1° than those with α=6.2°. The Mach number distribution in the upper region of the body shows some differences with respect to that obtained with M = 2.30.
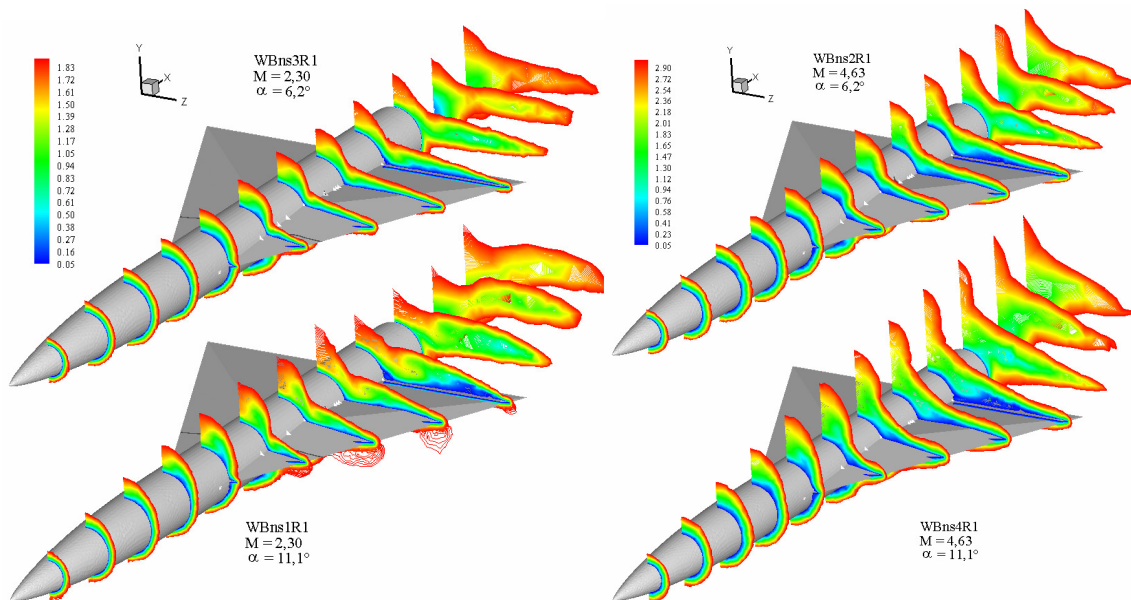
Figure 9: Mach number distribution over a W-B configuration for M=2.3 (left) and M=4.63 (right)

The pressure coefficient (Cp) distribution, presented in Figure 10, shows the influence of the Mach number and angle of attack for different stations (x/C_r) over the W-B configuration. The coordinate x is normalized with respect to the root chord C_r and the origin is located in the leading edge. As expected, the pressure coefficient increases with the angle of attack and

its growth is greater on the lower surface of the delta wing. The pressure coefficient is larger in the leading edge due to the detached shock wave.
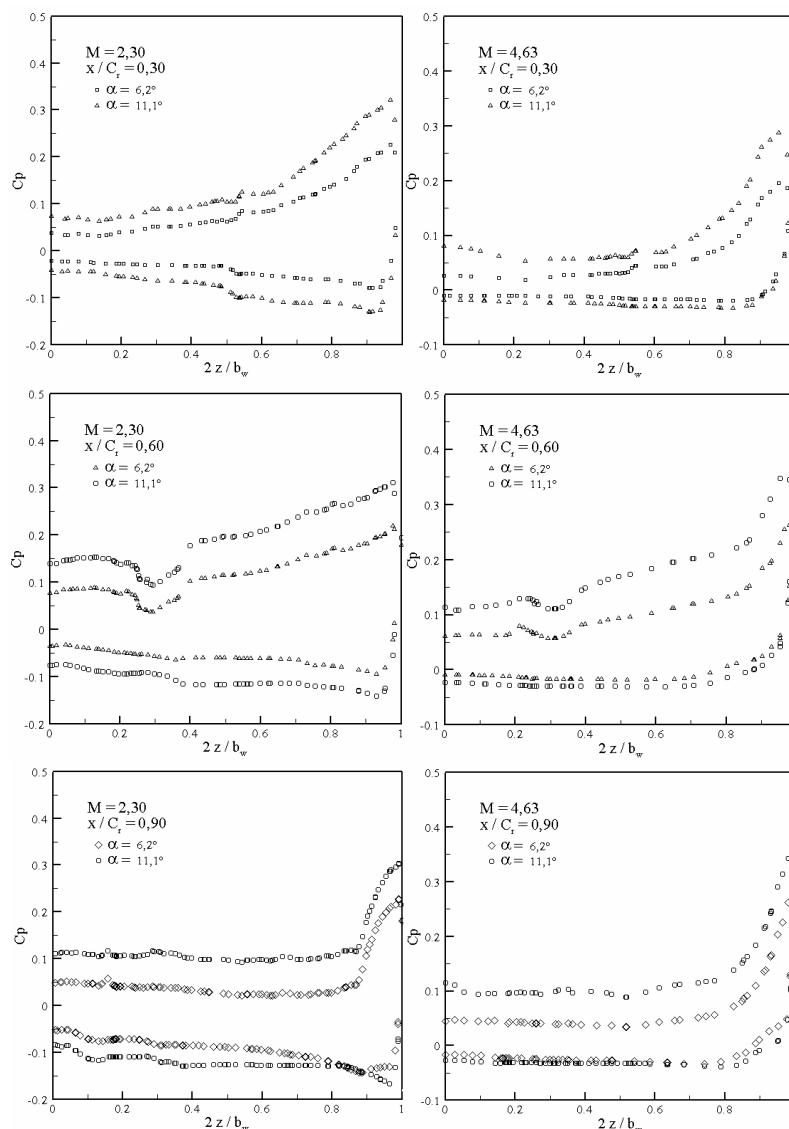
Figure 10: Pressure coefficient distribution over a W-B configuration for M=2.3 (left) and M=4.63 (right) with angle of attack 6.2° and 11.1°

On the lower surface of the wing (rear region) a reduction in the pressure coefficient is observed because the flow is accelerated by the expansion fan in the region of maximum thickness of the wing. It should be noted that for the same stations and angles of attack the pressure coefficient is always lower with the highest Mach number. The reduction of the Cp with the Mach number increase is in essence explained by the principle of independence of the Mach number (Anderson, 1989).

The pressure coefficient distributions over the W-B configuration for M=2.30 and M=4.63 are shown in Figure 11 and 12. It should be observed that the change in the pressure coefficient on the upper surface is smaller when the angle of attack increases, for M=2.30. Nevertheless, for M=4.63 no important changes are observed (see Figure 12).
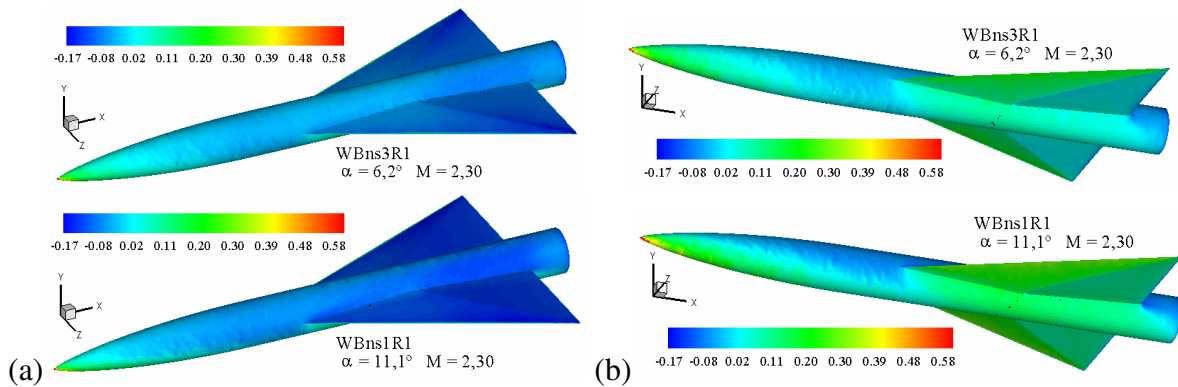
Figure 11: Pressure coefficient distribution over a W-B configuration for M = 2.3 with angle of attack 6.2° and 11.1°. (a) Upper surface, (b) Lower surface
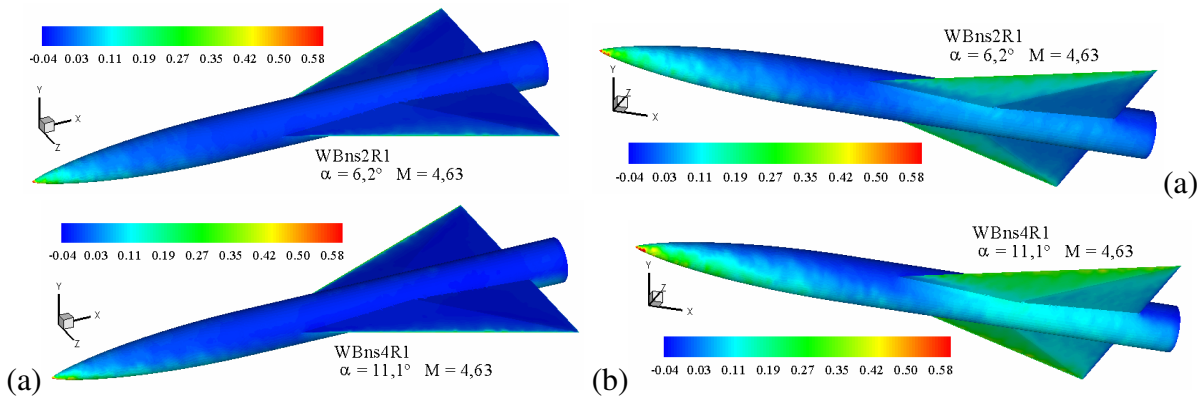
Figure 12: Pressure coefficient distribution over a W-B configuration for M = 4.63 with angle of attack 6.2° and 11.1°. (a) Upper surface, (b) Lower surface

Initially on the lower surface of the wing the flow is compressed (front region) and later expanded (rear region) reducing the pressure. The presence of the wing strongly influences the pressure distribution in the body, especially on the lower surface. In the W-B intersection, the pressure coefficient is modified in the leading edge region. It should be noted that the changes are important on the lower surface of the wing because the interaction is intense between the boundary layer of the fuselage and the shock wave of the wing.

Figure 13 shows the meshes and the isolines of Mach numbers in the plane *xy* for different Mach number-angle of attack combinations (all figures use the same Mach number scales for comparative purposes). It can be observed that elements are concentrated in regions where the physical phenomena present high gradients and low velocity. In the forebody region the results does not present a good resolution because the mesh does not provide a good transition between the different sizes of elements.

The specific mass distributions around the W-B configuration are presented in Figure 14. The shock wave formed at the nose and on the lower surface of the delta wing is efficiently captured as well as the expansion fan on the upper surface of the wing and the forebody region of the body. The shock on the lower surface diffuses more quickly than the shock on the upper surface because its initial strength is higher. It is observed that the adaptive method improves results in regions with low velocity and strong gradients; however near the rearbody region is less accurate because the initial mesh is relatively coarse in this region.
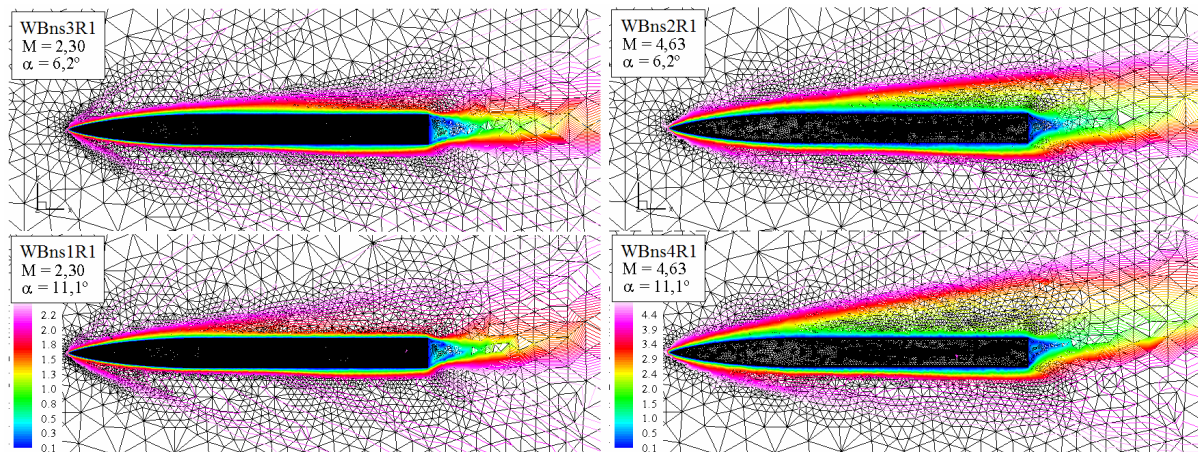
Figure 13: Meshes and Mach number distribution in the symmetric plane over a W-B configuration for M=2.30 and M=4.63 with angle of attack α=6.2º and α=11.1º
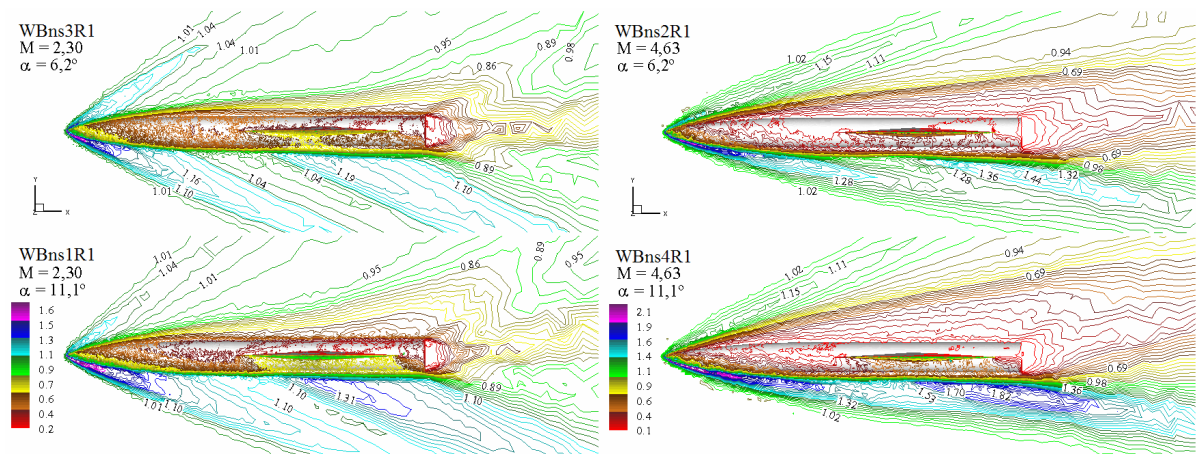
Figure 14: Specific mass distribution in the symetric plane over a W-B configuration for M=2.30 and M=4.63 with angle of attack alpha=6.2º and 11.1º

Finally, a comparative study of the formation and dynamics of vortices can be seen in Figure 15 at several longitudinal positions (x_b/L) along the W-B configuration with M=2.30 and M=4.63 and α = 11.1º. The flow field surrounding the W-B configuration is extremely complex, and some features such as multiple vortices influencing the W-B surface pressures are observed. For x_b/L = 0.50, it is observed, for both Mach numbers, two small vortex on the upper and lower W-B intersection region and a bigger vortex on the upper body region. The vortex over the wing grows in size for x_b/L=0.80 and x_b/L=0.90; it should be noted that for M=2.30 the vortices on the top of the wing and body tend to come together forming only one vortex. However, for M=4.63 two well defined vortices are observed.
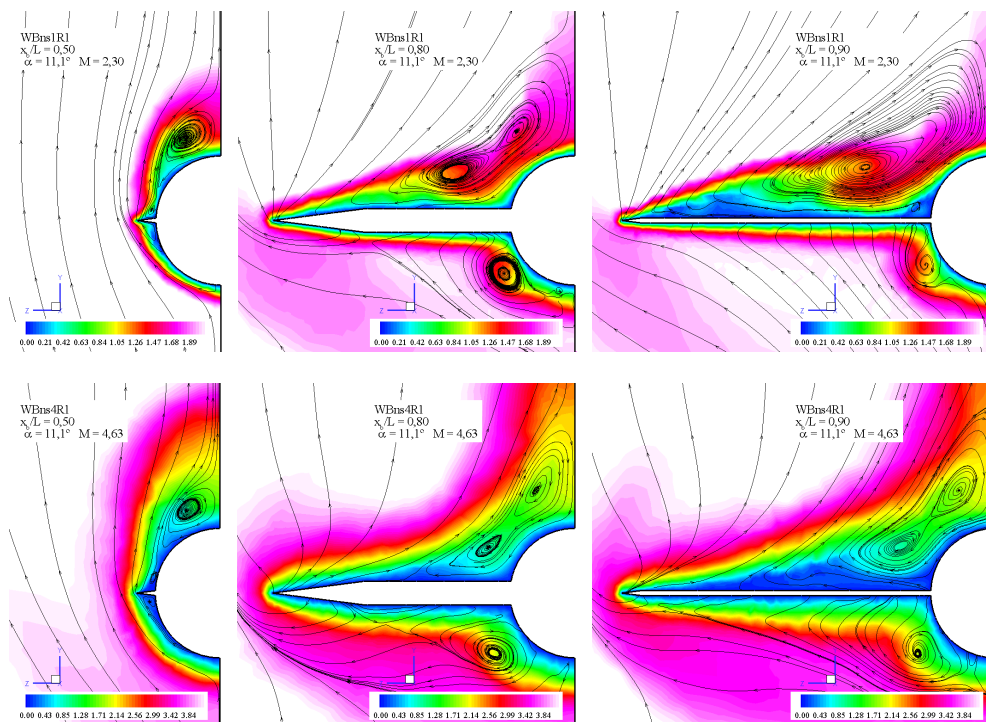
Figure 15: Mach number contours and streamlines in a cross flow plane over a W-B configuration for M=2.30 and 4.63 with angle of attack 11.1°

5.3 Aerodynamic coefficients

The surface pressures computed from the Euler/Navier-Stokes solver are integrated to determine the drag (*CD*), lift (*CL*) and pitching moment (*CMz*) coefficients. Experimental data are not available for this configuration. The aerodynamic coefficients are reported in Table 3. It is considered as reference values the coefficients at the wing surface and the span wing. The pitching moment coefficient is taken at coordinates (1.0, 0.0, 0.0).

cases	mesh	*CD*	*CL*	*CMz*
M=2.30 α=6.2°	WBns3	0.0677	0.293	0.293
	WBns3R1	0.0597	0.316	0.313
M=2.30 α=11.1°	WBeu1	0.1368	0.563	0.497
	WBeu1R1	0.1492	0.621	0.540
	WBeu1R2	0.1624	0.684	0.566
	WBns1	0.1385	0.516	0.505
	WBns1R1	0.1347	0.549	0.537
M=4.63 α=6.2°	WBeu2	0.0262	0.170	0.150
	WBns2	0.0463	0.178	0.156
	WBns2R1	0.0591	0.290	0.274
M=4.63 α=11.1°	WBns4	0.0955	0.336	0.294
	WBns4R1	0.1362	0.528	0.487

Table 3: Aerodynamic coefficients for the W-B configuration.

The Euler equations predict a slightly higher lift, drag and moment compared to the Navier-Stokes predictions for the case with M=2.30 and α=11.1°, but for the case where M=4.63 and α=6.2° greater values are obtained with the Navier-Stokes equations.

6   CONCLUSIONS

Euler and Navier-Stokes simulations were applied to a Wing-Body configuration in supersonic regime (M=2.30 and M=4.63). These simulations have been performed at moderate angles of attack (α=6.2° and α=11.1°) to examine the flow field characteristics, where vortices, shocks and separated flows occurs.

An explicit one-step Taylor-Galerkin scheme has been successfully used to predict the aerodynamic coefficients and flowfields on a Wing-Body configuration. The solutions with adaptive meshes capture the main flow structure characteristics, as it is demonstrated by comparisons with experimental data. The results of these computations provide valuable insight into the physics of the complex flows around Wing-Body configurations.

The present study should be extended introducing a turbulence model to accurately predict the effect of Reynolds number in this configuration. This is one of the key areas where CFD can fill a crucial gap in aerodynamic database for any aircraft design effort.

REFERENCES

Anderson, J.D. Jr. *Hypersonic and High Temperature Gas Dynamics*, McGraw-Hill Inc., USA, 1989.

Argyris, J., Doltsinis, I.S. and Friz, H.. Study on computational reentry aerodynamics. *Computer Methods in Applied Mechanics and Engineering*, 81:257–289, 1990.

Bertin, J.J. *Hypersonic Aerothermodynamics*, AIAA Education Series, USA , 1994.

Bono, G.. *Simulação Numérica de Escoamentos em Diferentes Regimes utilizando o Método dos Elementos Finitos (text in portuguese)*. Doctoral Thesis, PROMEC, UFRGS, Brazil, 2008.

Bono, G., Popiolek, T.L. and Awruch, A.M. Estrategia de Adaptación de Mallas para Problemas Aeroespaciales y Aeronáuticos, *Mecánica Computacional*, 26, 3117-3133, 2007.

Donea, J. A Taylor-Galerkin for convective transport problems. *International Journal for Numerical Methods in Engineering*, 20:101–119, 1984.

Hughes, T.J.R. and Tezduyar, T.E. Finite element methods for first-order hyperbolic systems with particular emphasis on the compressible Euler equations. *Computer Methods in Applied Mechanics and Engineering*, 45:217–284, 1984.

Jernell, L.S. Comparisons of theoretical and experimental pressure distributions over a wing-body model at high supersonic speeds, *TN D-6480, NASA*, 1971.

Löhner, R. *Applied CFD Techniques. An Introduction based on Finite Element Methods*. John Wiley & Sons Ltd., England, 2001.

Löhner, R., Morgan, K. and Zienkiewicz, O.C. The Solution of Non-linear Hyperbolic Equation Systems by the Finite Element Method. *International Journal for Numerical Methods in Fluids*, 4: 1043-1063, 1984.

Pirzadeh, S.Z. Vortical Flow Prediction Using an Adaptive Unstructured Grid Method. *RTO Meeting Proceedings 69(I), Symposium on Advanced Flow Management, NATO*, 2001.

Popiolek, T.L. and Awruch, A.M. Numerical Simulation of Incompressible Flows using Adaptive Unstructured Meshes and the Pseudo-compressibility Hypothesis. *Advances in Eng. Soft.*, 37: 260-274, 2006.